Influence of surface oxide characteristics and speciation on corrosion, electrochemical properties and metal release of atomized 316L stainless steel powders

Int. J. Electrochem. Sci., 7 **(2012)** 11655 - 11677

International Journal of
ELECTROCHEMICAL
SCIENCE
www.electrochemsci.org

Influence of Surface Oxide Characteristics and Speciation on Corrosion, Electrochemical Properties and Metal Release of Atomized 316L Stainless Steel Powders

Y. Hedberg[1,*], *M. Norell*[2], *P. Linhardt*[3], *H. Bergqvist*[4], *I. Odnevall Wallinder*[1]

[1] KTH Royal Institute of Technology, Div. Surface and Corrosion Science, Dept. Chemistry, Drottning Kristinas väg 51, SE-10044 Stockholm, Sweden
[2] Materials and Manufacturing Technology, Chalmers University of Technology, SE-412 96 Gothenburg, Sweden
[3] Institute for Chemical Technologies and Analytics (CTA), Vienna University of Technology, Getreidemarkt 9/164, A-1060 Vienna, Austria
[4] KTH Royal Institute of Technology, Div. Functional Materials, Dept. Material Physics, Electrum 229, SE-16440 Kista, Sweden
[*]E-mail: yolanda@kth.se

Received: 22 September 2012 / *Accepted:* 4 November 2012 / *Published:* 1 December 2012

Surface oxide characteristics of powder particles are important to consider for any toxicological risk assessment based on in-vitro or in-vivo tests. This study focuses on a multi-analytical approach (X-ray photoelectron spectroscopy, Auger electron spectroscopy, scanning- and transmission electron microscopy, and different electrochemical techniques) for in-depth characterization of surface oxides of inert-gas-atomized (GA) AISI 316L stainless steel powder, compared with massive sheet and a water-atomized (WA) 316L powder. Implications of differences in surface oxide phases and their surface distribution on corrosion, electrochemical properties and metal release are systematically discussed. Cr was enriched in an inner surface layer for both GA powders, with Mn and S enriched in the outermost surface oxide. The surface oxide was 2-5 nm thick for both GA powder size fractions, amorphous for the GA powder sized <4 µm and partially crystalline for the powder sized <45 µm. A strong ennoblement, i.e. positive shift in open circuit potential, of up to 800 mV, depending on solution, was observed for the GA powders. This ennoblement was induced by catalytic oxygen reduction properties of tri- or tetravalent Mn-oxides, not present on the massive sheet or WA powder. In contrast to the predominant presence of a trivalent Cr-oxide in the surface oxide of the GA powder particles, the WA<45µm powder revealed oxidized Cr, most probably present in its hexavalent state (not chromate), within a silicate-rich surface oxide. This study clearly shows that the surface oxide composition and speciation of differently sized GA and WA powders are unique (strongly connected to the atomization process) and of large importance for their pitting corrosion and metal release properties. For the GA<45µm powder, Mn-rich oxide nanoparticles were proposed to account for its higher pitting corrosion susceptibility, a more stable surface ennoblement, and a shift of the MnO_2 oxidation/reduction peaks in the cyclic voltammogram, compared with the GA particles sized <4µm.

The thermodynamically unstable ferritic structure of the small sized particle fraction (GA <4μm), despite an austenitic composition, revealed a higher pitting corrosion susceptibility and higher nickel release compared with the austenitic particle fraction of the GA <45 μm powder.

Keywords: surface oxide, speciation, characterization, manganese dioxide, oxide nanoparticles

1. INTRODUCTION

Within risk assessments of materials, the toxicity of a ”substance” is often classified according to standardized in-vitro or in-vivo tests. REACH (Registration, Evaluation, Authorisation and Restriction of Chemicals) [1-2] obligates all producers within the EU (European Union), or exporters into EU, to show that their substances or products are classified and safe from both an environmental and health perspective, “No data no market”. The responsibility lies hence on the industry to compile and/or generate data if lacking. The lack of metal release data and its possible correlation to surface characteristics and toxic response resulted recently in the generation of a substantial set of data within this area as a complement to findings in the scientific literature that enabled classification and risk assessment of ferrochromium alloys including stainless steel [3-11]. However, most recognized standard in vitro tests are based on studies of powders instead of massive surfaces, assuming the powder shape to mimic the behavior of massive sheet [6, 12]. Except for the fact that the production route of metal powders is very different, with variations in surface characteristics as a consequence, the generation of powders from massive sheet (commonly done) may furthermore not be representative for their intended use and also change the material/surface characteristics. Reproducible surfaces of powder particles are difficult to accomplish since they cannot be easily polished or prepared [13-15]. Previous findings have shown significant differences in the metal release behavior of differently sized powder particles of stainless steel, an effect partly connected to differences in surface oxide characteristics [13].

Surface oxide characterization is commonly made by using different analytical techniques including XPS (X-ray Photoelectron Spectroscopy), AES (Auger Electron Spectroscopy), SEM/TEM (scanning/transmission electron microscopy), EBSD (electron backscattered diffraction) and XRD (X-ray Diffraction). These techniques are limited in terms of either spatial or lateral resolution or chemical information of phases, and hence often combined. Reported findings show that the surface oxide (composition, phases/inclusions and their distribution, thickness etc.) of metal powders is connected to the cooling rate during atomization [16], the particle size and secondary dendrite arm spacing [16-18], the type of atomization (e.g., water-, gas-atomization, or rotating electrode process) [18], and the oxygen availability [19]. Minor elements with higher oxygen affinity, such as Mn, Si and Cr are often enriched at the surface, either as “oxide particles” or “islands” within or on a more continuous surface oxide of different composition (“matrix oxide”). This surface enrichment increase with reduced particle size [17-21]. Cr_2O_3 with MnO and Fe_2O_3 phases in the outermost surface layer [21], possibly combined with $MnCr_2O_4$, $FeCr_2O_4$, or $(Fe,Cr)_2O_3$ as particles or small local surface phases [22], have been reported for nitrogen atomized AISI 304L powders. Austenitic stainless steel powders may also

show a ferritic structure and/or solidify as single crystals if the cooling rate is rapid enough [23-26], as previously observed for the inert-gas-atomized 316L powder particles sized <4 µm of this study [14].

Electrochemical investigations are another way to identify and characterize oxide phases within, or on, powder particles. Oxide phases on micron-sized particles immobilized on paraffin-impregnated electrodes (PIGE) have been characterized using voltammetry [27-29]. Another method, that in addition is able to analyze dissolved ions, is the carbon paste electrode (CPE) with higher sensitivity than PIGE. CPE has been widely used to identify different metal oxide/hydroxide phases [30-35]. The benefit of electrochemical analysis of oxide phases, compared with surface analytical methods, is the direct information on their reduction/oxidation behavior, important information for considerations of corrosion and/or metal release mechanisms. It was recently shown that the oxide properties of inert-gas-atomized AISI 316L particles (sized <45 µm, the same as investigated in this paper) were crucial for their corrosion behavior, when compared to polished particles and massive sheet (part II of this paper series, [36]).

The aim of this paper is to employ a multitude of analytical techniques (XPS, AES, SEM, TEM) combined with different electrochemical methods (Open circuit potential measurements-OCP, Potentiodynamic polarization and cyclic voltammetry-CV) to characterize differences in surface oxide characteristics and corrosion properties of inert-gas-atomized AISI 316L stainless steel powders compared with massive sheet and a water-atomized 316L powder. The inert-gas-atomized AISI 316L powders have previously been investigated at in-vitro [4-5, 8-9, 13, 37] and in-vivo [15] conditions. The influence of surface oxide characteristics and composition on the corrosion properties, extent of metal release and the electrochemical (catalytic) properties are discussed from a mechanistic perspective.

2. MATERIALS AND METHODS

2.1. Materials

Table 1. Nominal composition of gas-atomized (GA) and water-atomized (WA) 316L powders, sized <4 and <45 µm, respectively, and massive sheet.

	Fe (wt%)	Cr (wt%)	Ni (wt%)	C (wt%)	Si (wt%)	Mo (wt%)	Mn (wt%)	S (wt%)	Cu (wt%)
GA<45µm	68.90	16.80	10.30	0.03	0.50	2.10	1.40	0.01	-
GA<4µm	65.50	18.50	11.60	0.05	0.65	2.30	1.40	0.008	-
WA<45µm	66.36	17.13	13.14	0.02	0.86	2.30	0.11	0.008	0.05
Massive 316L	69.3	16.6	10.6	0.03	0.4	2.1	1.0	0.001	-

Nominal bulk alloy compositions of the investigated AISI 316L massive sheet (produced by Thyssen Krupp, Germany), the gas-atomised 316L powder sized <45 µm (GA<45µm, produced by ANVAL, Torshälla, Sweden), the gas-atomized 316L powder sized <4 µm (GA<4µm, produced by

Sandvik Osprey Limited, UK), and the water-atomized 316L powder sized < 45 µm (WA<45µm, produced by Höganäs AB, Sweden) are compiled in Table 1. The test materials were supplied via the European Confederation of Iron and Steel Industries and International Stainless Steel Forum, Belgium.

Information on the specific surface area, measured by means of the BET method (nitrogen adsorption at cryogenic conditions) has been described previously [4] and is summarized in Table 2.

Table 2. Specific surface areas, measured by means of the BET method, of the different 316L powders (GA: gas-atomized, WA: water atomized).

Stainless steel 316L powders	BET specific surface area (m^2/g)
GA<4µm	0.700
GA<45µm	0.069
WA<45µm	0.087

Particle size distribution values of the three powders in phosphate buffered saline (PBS, 8.77 g/L NaCl, 1.28 g/L Na_2HPO_4 and 1.36 g/L KH_2PO_4, pH 7.2-7.4) measured by means of low angle laser light scattering (LALLS, using a Malvern Mastersizer 2000 equipment with a Hydro SM dispersion unit, experimental details in [4]) is shown in Table 3.

Table 3. Particle size distribution of the stainless steel powder particles in phosphate buffered saline (PBS) measured by means of LALLS. $d_{0.5}$ is the median particle diameter and $d_{0.1}$ and $d_{0.9}$ the 10 % and 90 % size distribution cut off points by volume (mass) or number, respectively.

	Unit	GA316L <4µm	GA316L <45µm	WA316L <45µm
Volume / diameter - µm	$d_{0.1}$	2.25 ± 0.05	10.61 ± 0.24	18.46 ± 0.02
	$d_{0.5}$	3.91 ± 0.09	21.37 ± 0.82	35.47 ± 0.12
	$d_{0.9}$	6.63 ± 0.17	38.95 ± 1.52	64.76 ±0.24
Number / diameter - µm	$d_{0.1}$	1.58 ± 0.03	2.04 ± 0.19	11.08 ± 0.04
	$d_{0.5}$	2.35 ± 0.04	3.74 ± 0.70	17.61 ± 0.03
	$d_{0.9}$	3.97 ± 0.08	14.22 ± 0.61	32.42 ± 0.04

2.2. Analytical techniques

2.2.1. X-ray photoelectron spectroscopy (XPS)

Compositional analysis of surface oxides of the powders was performed by means of XPS (UltraDLD spectrometer from Kratos Analytical) using a monochromatic Al x-ray source (150 W) on

areas approximately sized 700 x 300 µm. Wide spectra were run to detect elements present in the outermost surface oxide (information depth of a few nm) at five different locations, and detailed high resolution spectra (20 eV pass energy) were acquired for the main compositional elements. The binding energy of the C 1s (C-C, C-H) signal (285.0 eV) was used as internal reference. The Fe 2p peak was separated according to its metallic (706.9±0.25 eV) and oxidized (711.9±1.2 eV) states. No metallic chromium, only oxidized (576.8±0.71 eV) chromium was detected. Oxidized manganese was detected at binding energies of 641.6±0.2 and 644.0±1.0 (GA<4µm) and 641.4±0.05 and 643.1±0.01 eV (GA<45µm). No metallic or oxidized nickel was detected. Oxidized silicon was only detected in the case of the WA powder at a binding energy of 102.6±0.2 eV (as silicate [38]). Results obtained by means of XPS are reported in [39], but included for comparative reasons.

2.2.2. Auger electron spectroscopy (AES)

The composition and thickness of the oxide on individual GA powder particles were determined by means of AES depth profiling (MicroLab 350 from Thermo Scientific). Sensitivity factors from the manufacturer were used for apparent quantification. The powder was mounted by gently pressing a quantity between pure Al plates. The powder analyzed has not been in contact with the Al plates. The rate of Ar^+-etching was calibrated on Ta_2O_5 films of known thickness. This rate varies with the angle of ion incidence and this was considered as described elsewhere [40]. In short, the spherical shape of the particle is used to geometrically determine an area of analysis where the angle of ion incidence gives a maximal etch rate as calibrated. The width of this area is approximately 15% of the particle radius. If the area of analysis deviates from the ideal position, or the particle is not totally spherical, the etch rate will be slower than that calibrated and the oxide thickness hence overestimated. This is of importance for the very small particles studied in this study. On GA<45µm, the area of analysis was about 1 µm in square. On GA<4µm, point analyses were done with a lateral resolution of approximately 20 nm. The ideal etch position on the typically 1 µm large particles analyzed was about 75 nm wide. Therefore, any drift in the SEM image during profiling may have resulted in an overestimated oxide thickness on some particles. Thus, the thinnest oxide thickness determined is the most reliable.

2.2.3. Transmission electron microscopy (TEM)

The GA<4µm powder was prepared by first mixing the powder particles in an electron beam compatible epoxy resin (Gatan Inc. US). This mixture was cast within brass tubes (outer Ø - 3 mm). The tube was cut to 0.6 mm thick slices. These slices were ground on silicon carbide paper with final grinding on grade 4000 mesh down to a thickness of 0.1 mm. The thin slices were dimpled by using a dimple grinder (Gatan Inc., US model 656) using diamond paste, and at the last step in a SiO_2 water slurry. In order to minimize the time for the ion polishing, it was essential to calculate the final minimum thickness which should be as thin as possible. Finally, thinning to electron transparency was performed by using a precision ion polishing system (PIPS, Gatan Inc. US) and by using a

successively lower acceleration voltage ranging from 3.5 kV down to 1.5 kV. The GA<45μm powder was prepared by using a focused ion beam, FIB (FEI model QUANTA 3D FEG). The powder particles were attached to a double-sided adhesive carbon based disc. One representative particle was sputtered with platinum for protection on an area sized approx. 25 x 5 μm^2, and cut with a Ga-ion beam down to a thickness corresponding to electron transparency. Finally, the sliced foil was cut and attached on a TEM-grid.

The sliced foils were examined by means of TEM (JEOL 2100F (HR)) equipped with scanning transmission electron microscopy (STEM), energy dispersive x-ray spectrometry (EDXS) and electron energy loss spectroscopy (EELS). The surfaces of the particles were imaged in high magnification with lattice resolution in order to characterize the crystal structure and the amorphous degree of the surface oxide. EDXS analyses were performed to measure the concentration of different elements in the surface oxide. Point analyses (a few nm resolution) at different locations and line scans were performed. By using this method a detection limit of 0.1% of different elements was possible to achieve.

2.2.4. Field emission gun scanning electron microscopy (FEG-SEM)

High resolution morphology studies were performed by means of field emission gun scanning electron microscopy (FEG-SEM Leo1530 upgraded to Zeiss Supra 55) up to 100,000 times magnification using secondary electrons, a working distance of 5.7 mm, and a voltage of 10 or 15 kV. The powders were fixed on carbon tape.

2.3. Electrochemical techniques

2.3.1. Open circuit potential (OCP) measurements

OCP was measured as a function of pH, solution, and time. Both massive sheet and powders were investigated. The massive sheet was abraded to 1200 SiC grit, consecutively and ultrasonically cleaned with acetone for 7 min and isopropyl alcohol for 7 min, prior to storage for 24 h ± 1 h in a desiccator. The powder (approx. 4 mg) was immobilized on a paraffin-impregnated graphite electrode (PIGE), with an area of approx. 0.5 cm^2, which was abraded and shortly heated prior to pressing it into the powder for fixation. The PIGE background current has previously been found to be significantly lower compared to the current of the PIGE and of the investigated particles [36, 41]. The massive sheet, of which approximately 1 cm^2 was immersed in solution, was fixed using a clamp (not immersed). The counter electrode was a platinum wire and Ag/AgCl 3M KCl was used as the reference electrode. The pH dependent OCP measurements were performed for massive sheet, and powders of GA<45μm, GA<4μm, and MnO_2 (specific surface area (BET) of 0.054 m^2/g, Sigma Aldrich, Lot no. MKBC2119V) as reference. The manganese concentration of the buffer solution was adjusted to 1 mg/L Mn^{2+} (as this is well above the expected release of manganese for the investigated time period [13]) which however precipitated to some extent in the case of pH 10.1. The buffer solutions (from [42]) for the different pH values were prepared as follows: 0.1 M CH_3COOH and 0.1

M $NaCH_3COO$ (pH 4.7), 50 mL 0.1M KH_2PO_4 and 5.4 mL 0.1 M NaOH in 100 mL (pH 6.0), 50 mL 0.1 KH_2PO_4 and 32 mL in 100 mL (pH 7.0), 50 mL 0.1 M KH_2PO_4 and 46.1 mL 0.1 M NaOH in 100 mL (pH 7.8), and 50 mL 0.05 M $NaHCO_3$ and 10.7 mL 0.1 M NaOH in 100 mL (pH 10.1). All measurements were performed by allowing the OCP to stabilize for 1 h, or after a change in potential being less than 10 μV/s, before the value was recorded.

The influence of solution on OCP was investigated for massive sheet, GA<45μm, GA<4μm, and WA<45μm powders, in solutions relevant for metal release studies into synthetic body fluids, i.e. gastric fluid (GST, pH 1.5-1.7, 4 g/L 25% HCl), artificial lyosomal fluid (ALF, pH 4.5, 20.8 g/L $C_6H_8O_7$, 6.00 g/L NaOH, 3.21 g/L NaCl, 0.050 g/L $MgCl_2$, 0.071 g/L Na_2HPO_4, 0.039 g/L Na_2SO_4, 0.128 g/L $CaCl_2 \cdot 2H_2O$, 0.077 g/L $C_6H_5Na_3O_7 \cdot 2H_2O$, 0.059 g/L H_2NCH_2COOH, 0.090 g/L $C_4H_4O_6Na_2 \cdot 2H_2O$, 0.085 g/L $C_3H_5NaO_3$, 0.086 g/L $C_3H_3O_3Na$, 1.7 mL/L 50% NaOH), 3 g/L NaCl (not pH adjusted, pH approximately 5.4-7), and 8 M NaOH (pH 13.1-13.3). The influence of time was investigated in GST for up to 48 h, for massive sheet, GA<45μm, GA<4μm, and WA<45μm. All measurements were made at aerated conditions, with the exception of half of the measurements investigating the pH dependence, where nitrogen gas was purged through the solution prior to the measurement and blown on the solution during the measurement.

2.3.2. Potentiodynamic polarization

Anodic polarization curves, starting at OCP (after stabilization) and ending at 1.2 V vs. Ag/AgCl 3 M KCl with a scan rate of 0.2 mV/s were run for the powders of GA<45μm, GA<4μm, and WA<45μm in 0.03 M HCl (5 g/L 25% HCl). This solution has previously found to be sufficiently aggressive to enable observations of differences between the different powders investigated [41]. The GA<45μm powder was in addition separated into a magnetic (ferritic) and a non-magnetic (austenitic) particle fraction and investigated using anodic polarization.

2.3.3. Cyclic voltammetry (CV)

Cyclic voltammetry starting at OCP, polarizing cathodically to approx. -1.2 V and consecutively polarizing anodically to approx. +0.4 V, in 8 M NaOH, was performed to identify the presence of any oxidized metal phases. Powders of GA<45μm, GA<4μm, WA<45μm, and abraded particles (abraded from a massive sheet of 316L using a clean diamond file) stored for at least 24 h at ambient conditions ("massive" particles) were investigated using a carbon (graphite) paste electrode (CPE) and a reference electrode of Hg/HgO in 8 M NaOH, as previously described [43]. The scan rate was set to 0.5 mV/s. Powder concentrations in the graphite paste are given in Fig. 8. Different concentrations were investigated as the powder concentration has previously been shown to significantly influence the spectrum [43]. In order to obtain representative spectra, differences in BET area were taken into account.

3. RESULTS AND DISCUSSION

3.1. Surface oxide characteristics and composition based on a multi-analytical approach

3.1.1. XPS, outermost surface oxide composition

The surface elemental composition of the gas- and water atomized 316L powders based on XPS is compiled in Table 4. As previously reported [39], no accurate assignment of di- and tri-valent Fe oxidized species was possible due to overlapping binding energies. In accordance with literature findings [16-17], oxidized Si (most probably present as silicates [38]) was strongly enriched at the surface on the water-atomized particles, in addition with oxidized Mn (indicative of tri- and/or tetra-valent Mn-species, possibly MnO_2) [44] in the case of the gas-atomized powder. In both cases, these enrichments increased with reduced particle size [18]. There was a significant increase of the binding energy and peak width of oxidized Cr for the WA-powder compared to the GA-powders (trivalent Cr-species only) from 576.6±0.35 eV to 577.4±0.09 eV, which suggests a possible higher oxidation state. However, due to overlapping peaks between hexa- and tri-valent Cr-species, any accurate assignment was not possible. More speciation-sensitive techniques are required.

Table 4. Surface oxide composition (wt%) of gas-atomized (GA) and water-atomized (WA) 316L powder particles sized <4 and <45 µm, and massive sheet, measured by means of XPS. (Relative oxidized metal components only, the presence of carbon and oxygen is not taken into account).

	Mn	Fe	Cr	Si
GA<4µm	47±5	40±4	14±1	<LOD
GA<45µm	13±1	72±7	15±2	<LOD
WA<45µm	<LOD	24±2	17±2	59±6
Massive sheet	<LOD	75±8	25±3	<LOD

<LOD – below limit of detection

3.1.2. AES depth profiles and FEG-SEM investigations

Depth profiles by means of AES (for GA<4µm and GA<45µm) and high resolution images by means of FEG-SEM (all powders) are displayed in Figs. 1-3. Similar to XPS findings, carbon was present on the utmost surface but was disregarded as adventitious carbon contamination. The oxide thickness was estimated to approximately 2 nm for both powders, estimated from half the decay of the oxygen content. This was the thinnest oxide thickness recorded/estimated for each powder and also the most reliable measure (c.f. experimental section). Variations in thickness up to 3 nm were recorded for both powders. Selected depth profiles are shown in Fig. 1. In the case of the GA<45µm particles, other replicate measurements showed similar depth profiles, but slightly different oxide thicknesses. In the case of the GA<4µm particles, most profiles were similar to Fig. 1. Some particles revealed significantly different depth profiles, as discussed below.

Mn was clearly enriched at the utmost surface, Fig. 1, to a higher extent for the smallest particles, findings in agreement with the literature [18-19, 21]. In the case of the GA<4µm particles, the relative atomic percentage of Mn (total elements) ranged from 4, Fig. 1c, to 7 at% at the utmost surface, as compared to 1-2 at% for the larger powder, GA <45 µm. The absolute values of the AES depth profiles should though be interpreted with caution since the sensitivity factors are not exactly known. S was also enriched at the utmost surface and present up to a few nm into the surface oxide. This enrichment was more pronounced in the case of the GA<45µm particles compared with GA<4µm particles. The S depth profile did however not follow the same trend as observed for other elements such as Mn, which may suggest that it is not solely or necessarily present as MnS.

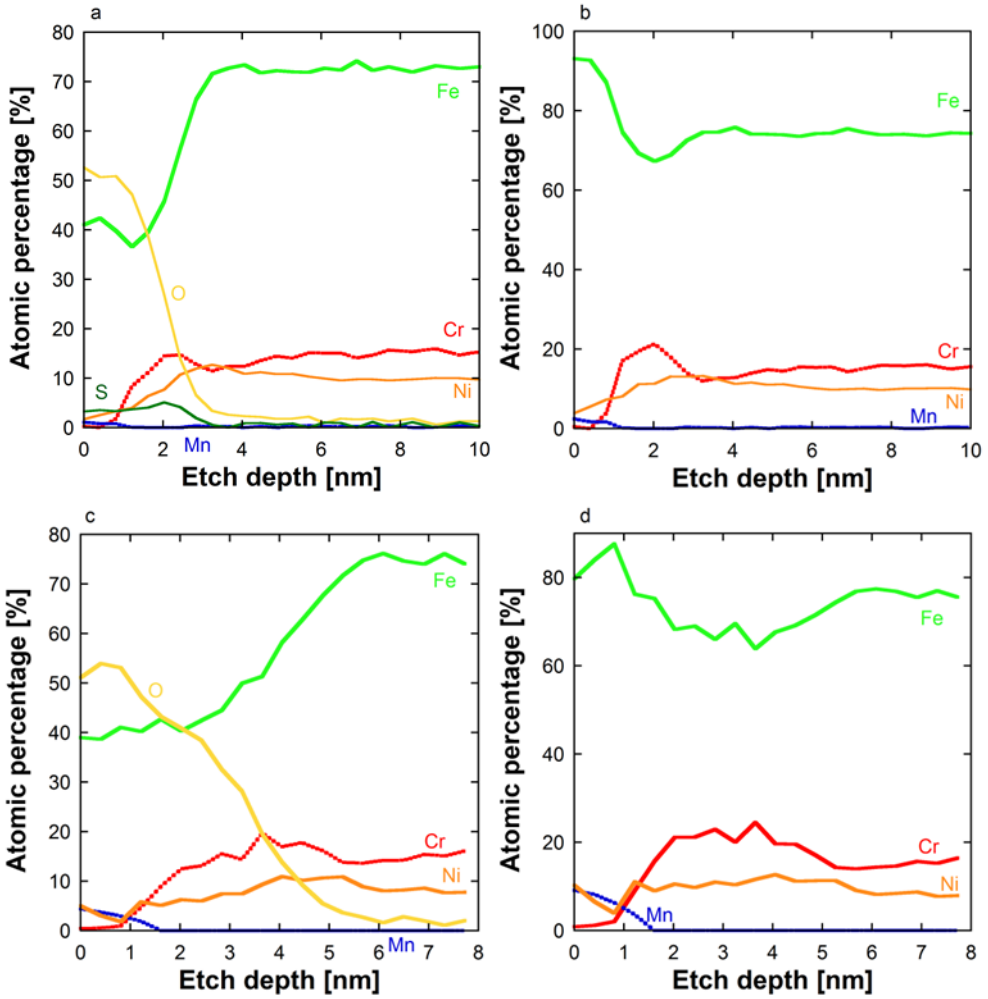

Figure 1. AES depth profiles (total elements, carbon excluded, left; cationic profile, right) for GA 316L particles sized <45µm (a, b) and <4µm (c, d).

In accordance with previous investigations of stainless steel powders [18, 21] oxides of Fe were the predominant components of the utmost surface whereas oxidized Cr only appeared further into the layer reaching a maximum concentration at the depth corresponding to the oxide thickness and always connected with a minimum in the iron content intensity. These observations were interpreted as an

inner Cr-rich oxide, in agreement with the literature [18] and an adjacent outer Fe-rich oxide. The maximum Cr concentration was more pronounced for the GA<45µm particles compared with the GA<4µm particles. For one particle out of ten GA<4µm particles analyzed, 6 at% Cr and 5 at% Ni were detected at the outermost surface (0 nm depth, data not shown). It was not possible to determine if Ni was in its oxidized or metallic state. However, no Ni was detected within the XPS measurements, providing average data for a large surface area and number of particles. These observations are in concordance with literature findings on gas-atomized 304L powders where Ni was not detected by XPS but still present in small amounts at the surface [21]. AES measurements also revealed the presence of small amounts of Cu (~2 at%) enriched at the utmost surface of two out of ten investigated GA<4µm particles (data not shown). Some of the GA<4µm particles mostly contained Ni and Cr (2 out of 10 particles).

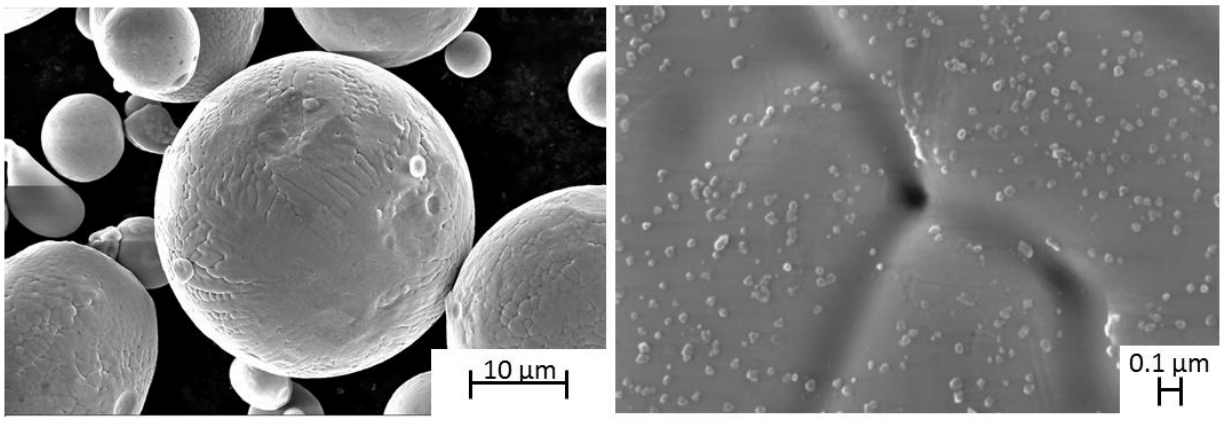

Figure 2. High resolution FEG-SEM images of inert-gas-atomized (GA) 316L <45 µm powder particles, showing their morphology, surface microstructure, grain boundaries and presence of surface oxide particles. Magnifications: 5,000 and 100,000 x.

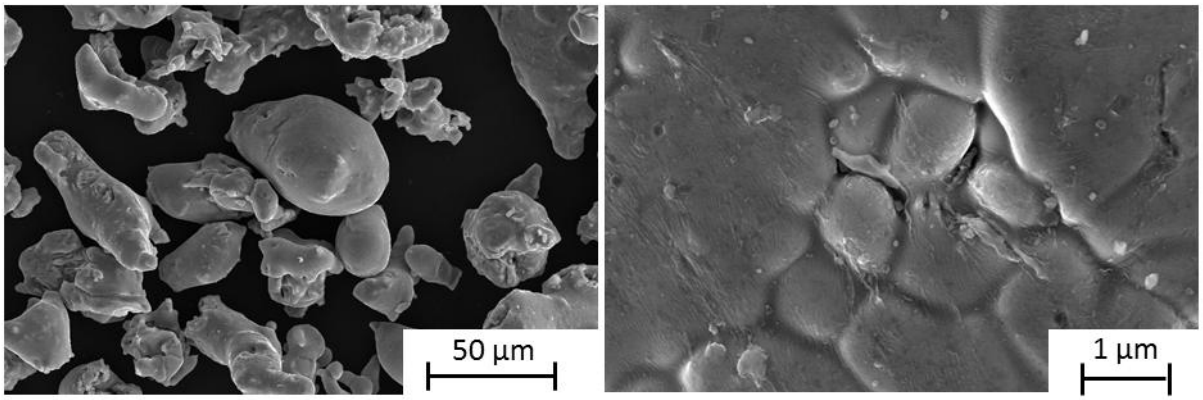

Figure 3. High resolution FEG-SEM images of water-atomized (WA) 316L <45 µm particles. Magnifications: 650 and 20,000 x.

The presence of such particles within the same GA<4µm powder has previously been observed by means of EDS (36 wt% Ni, 50 wt% Cr, 7.4 wt% Mo and 3.8 wt% Fe) [14]. The origin of these

particles is at present unknown, however possibly formed during the atomization process or impurities. Previous findings propose the initial formation of oxide particles with strong oxide formers such as Mn, Cr and Si [19-21, 45], and the subsequent formation of a Fe oxide [19, 21, 45] and/or Cr oxide [21] layer (and in the case of WA-particles an oxidized Si layer [46]) during atomization and handling. Oxide particles rich in Mn, Fe, and Si (based on EDS findings), have been reported for water-atomized particles [20]. Surface particles were observed also in this study for the powders sized <45µm, Fig. 2-3. These surface particles, approximately sized 20 nm up to a maximum size of 100 nm, were relatively homogeneously distributed on GA powder particles. For the WA powder, less abundant surface particles were observed, c.f. Fig. 3, compared to the GA powder, suggesting that most of the oxidized silicon (59 wt%, Table 1) was present within the continuous surface oxide. In the case of the GA<45µm powder, these oxide nanoparticles were investigated by means of AES point analysis, and compared with the matrix oxide as reported in [39]. The oxide nanoparticles were enriched in Mn, with approximately an equal amount of Fe and small amounts of S. These elements were not only present in these surface nanoparticles but also at further etching depth, suggesting relatively homogeneous oxide nanoparticles. In contrast, the outermost surface oxide surrounding these particles (matrix oxide) consisted only of Fe and O, with approximate ratio of 2:3, suggesting Fe_2O_3 [39]. No Mn or S was detected there [39].

3.1.3. TEM/EDXS investigations of surface oxide morphology, thickness and crystallinity

TEM (Fig. 4) combined with EDXS investigations of the GA<4µm and GA<45µm powders confirmed in general the oxide thickness estimation made by means of AES and the elemental distribution within the surface oxide, with the exception of the Mn content. Significantly lower relative amounts of Mn were determined with EDXS compared with both AES and XPS. However, this discrepancy was attributed overlapping peaks for Fe Lα and Mn Lα. In agreement with AES, Ni and Cr were less abundant at the utmost surface compared with Fe. Based on TEM findings, the oxide thickness varied at different investigated locations from approximately 2-3 nm to 5 nm for the GA<45µm particles, and was <5 nm for the GA<4µm particles, Fig. 4. The GA<4µm particles revealed an amorphous surface oxide without any surface oxide nanoparticles, Fig. 4a. In agreement with FEG-SEM and AES analyses, the GA<45µm powder revealed in contrast many differently sized surface nanoparticles (Fig. 4b). The surface oxide revealed both crystalline and amorphous areas, Fig. 4b.

The absence of surface oxide nanoparticles on the GA<4µm powder may be explained by their high cooling rate, during atomization, hindering their formation. A very rapid cooling rate for this powder is indicated by previous findings with a bulk structure of a frozen-in ferritic structure, a cellular microstructure (in contrast to dendrites for the GA<45µm powder) and many single-crystalline particles [14].

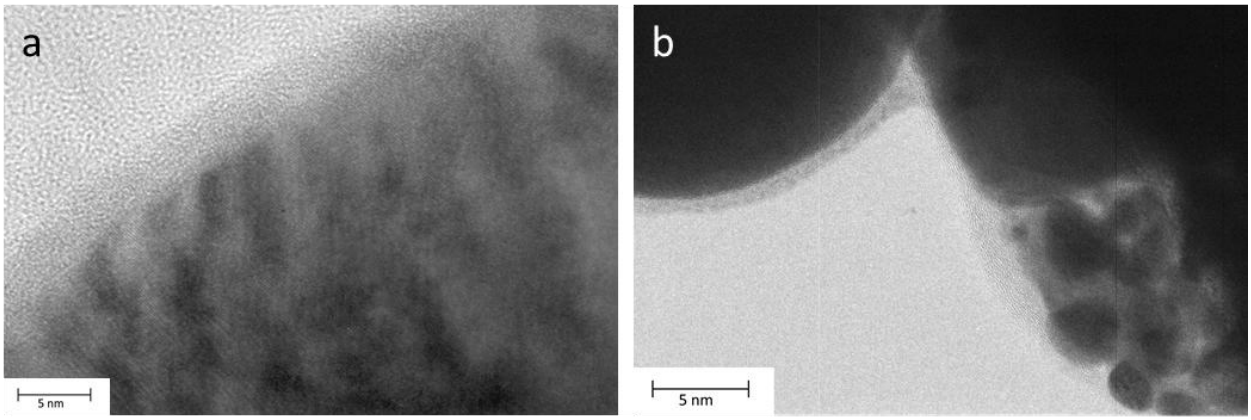

Figure 4. TEM images of the surface oxide of a) gas-atomized 316L powder <4µm and b) gas-atomized 316L powder <45µm. The light grey areas are the background, the slightly darker regions the oxide and the dark areas the metal (a), oxide nanoparticles and/or metal (b). The pattern in the metal region in (a) is caused by dislocations.

3.2. OCP measurements - Importance of oxidized manganese in the surface oxide

In parallel studies (part II of this paper series [36]), the GA<45µm powder showed a very high OCP prior to any applied current, being substantially higher (up to 800 mV) compared with the OCP after applying small reductive currents. This effect was only observed for non-polished powder particles, not for polished particles [36], which indicates the importance of the surface oxide formed already during the inert-gas atomization process. Based on XPS, AES, TEM and Raman [39] measurements, oxidized Mn-phases are the only possible constituents that may influence the OCP in this strong way. MnO_2 deposits on stainless steel have previously been reported to induce a similar ennoblement [47-51], i.e. a substantial shift of the OCP to more positive potentials.

To investigate if MnO_2 or any other trivalent or tetravalent Mn oxide/hydroxide species could explain the observed OCP shift for the GA<45µm powder, a series of investigations was initiated including studies of effects of pH, solution, and time on OCP, and cyclic voltammetry measurements to possibly identify any oxidized Mn phases. The pH dependence of the OCP of powders of MnO_2 (as reference), GA<4µm, and GA<45µm, and massive sheet is presented in Fig. 5. The massive sheet was abraded 24 h prior to the measurement and revealed typical OCP values at these conditions [49-50]. At pH 7, the following reaction is expected for MnO_2 [49]:

$$MnO_2 + 4H^+ + 2e^- \rightarrow Mn^{2+} + 2H_2O \qquad E^0 = +1.224\ V \qquad (1)$$

The Nernst's equation at pH 7 and a Mn(II) concentration ($c_{Mn(II)}$) of 1 mg/L, predicts a potential (E) of +341 $mV_{Ag/AgCl}$, and the theoretical pH dependence is -118 mV/pH at neutral and acidic pH. The measured OCP for the MnO_2 powder was 312.5±3.2 mV and a pH dependence of 103.5±3.5 mV/pH (both at aerated and deaerated conditions) was determined experimentally between pH 4.7 and 7.8 (Fig. 5). Between pH 7.8 and 10.1, a decreased pH dependence (67.5±3.5 mV/pH) was observed for the MnO_2 powder (both at aerated and deaerated conditions, Fig. 5). This is in accordance

with the theoretical shift to the one-electron transition between MnO_2 and MnOOH at higher pH values [49]. Observed OCP values of the GA powders were in-between observed figures for massive sheet and the MnO_2 powder, Fig. 5. The GA<45µm and GA<4µm powders revealed similar OCP values at neutral and alkaline pH, however, not at pH 4.7, where the OCP of GA<45µm was significantly higher compared to GA<4µm. The pH dependence of massive sheet of 78.5±0.5 mV/pH between pH 4.7 and 7.8 and 52.5±2.5 mV/pH was lower compared with the MnO_2 powder. The GA<45µm powder revealed a very similar pH dependence as MnO_2: 134.5±7.5 mV/pH between pH 4.7 and 7.8, and the GA<4µm powder somewhat lower values (74.5±16.5 mV/pH), close to the pH-dependence for massive sheet (78.5±0.5 mV/pH). No significant differences between deaerated and aerated conditions were observed for any of the powders or surfaces, in agreement with previous investigations of massive stainless steel and MnO_2 coated stainless steel [49]. Based on these pH dependent measurements, it can be concluded that significant positive shifts in OCP of the inert-gas-atomized powder occurred compared with the massive sheet, and were most probably caused by tri- or tetra-valent Mn-species. A reduced OCP for GA<4µm particles compared with GA<45µm particles at pH 4.7 indicated in addition that these species may be dissolved to different extent at these conditions.

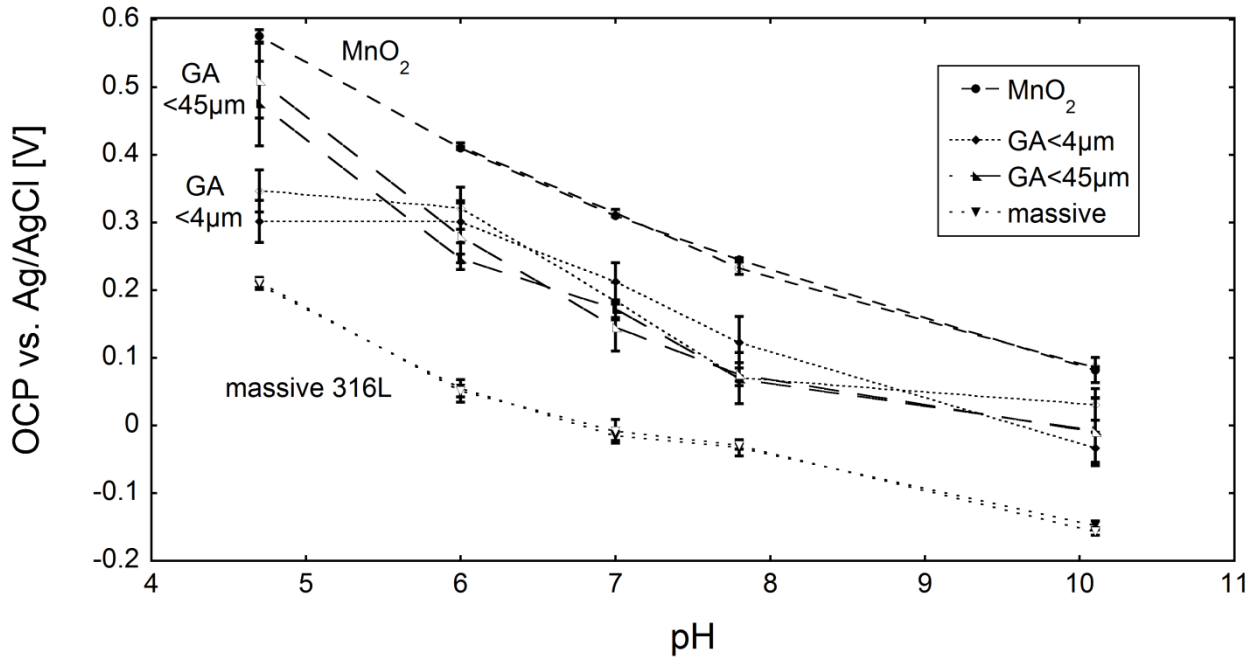

Figure 5. OCP values of massive 316L, inert-gas-atomized powders - GA 316L < 4 (GA<4µm) and < 45 µm (GA<45µm), and MnO_2 powder, in different buffer solutions containing 1 mg/L Mn(II), at both aerated (filled symbols) and deaerated (unfilled symbols) exposure conditions. The error bars represent the standard deviation between 2 and 5 independent measurements.

The effect of solution on OCP was investigated for the GA powders compared with massive sheet and the WA powder (without any oxidized Mn surface species). Studies were conducted in gastric fluid (GST) of low pH (1.5), artificial lysosomal fluid (ALF)-a highly complexing solution (pH 4.5) [13], 3 g/L NaCl (pH 5.4-7), and 8 M NaOH (pH 13.1-13.3), Fig. 6. In contrast to the influence of

pH, Fig. 5, the GA<45µm powder revealed a significantly more positive OCP compared to the GA<4µm powder in all solutions of a pH between 1.5 and 7. This may be attributed to the dissolution of surface-active Mn-species in the case of GA<4µm powder. Previous metal release studies in ALF revealed a significant enhancement of released metals from the GA<4µm powder compared with the GA<45µm powder. However, the opposite scenario was the case in low aggressive solutions [13]. The difference in OCP between the <4 µm and the <45 µm GA powders was 800 mV in the highly complexing ALF solution of low pH, Fig. 6. The same difference in OCP has previously been observed after applying small cathodic currents on the GA<45µm powder in 0.1 M HCl [36]. The oxidized Mn-phase on the GA<45µm powder particles seemed hence to be easily reducible when a cathodic current was applied, but not in any of the solutions at acidic or neutral pH within the investigated time-frame.

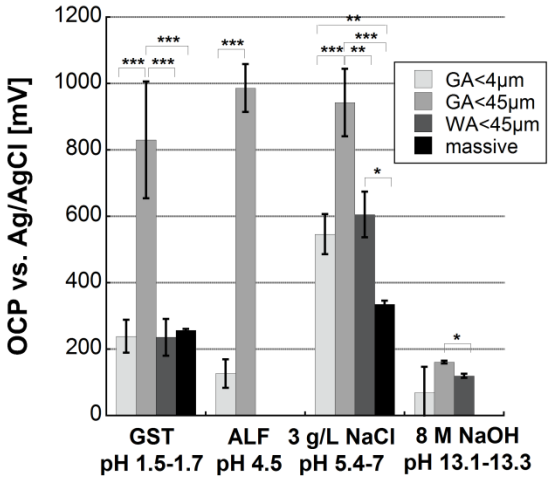

Figure 6. OCP values (after stabilization) of gas atomized GA 316L powders (< 4 and < 45µm), water atomized WA 316L powder <45µm (only in GST, NaCl, and NaOH), and massive 316L (only in GST and NaCl) in different solutions. The asterisks indicate significant differences within one solution, calculated by means of a student t-test (unpaired data with unequal variance): * for $p<0.05$, ** for $p<0.01$, and *** for $p<0.001$.

To investigate if the shift in OCP, induced by the presence of oxidized Mn-phases, was time-dependent, the OCP was recorded over time in GST (pH 1.7), Fig. 7. For both massive sheet and the WA<45µm powder (in two of three replicate samples, respectively), a "breakdown" was observed from initial OCP values of about 200 mV (Ag/AgCl) to values between -100 and -200 mV, Figs. 7a and b. This breakdown occurred earlier (after 0-50 s) for massive sheet compared to WA<45 powder (up to 1000 s), indicating somewhat more protective properties of the surface oxide of WA<45µm powder particles compared with the abraded (24 h prior to measurements) massive sheet. The GA<4µm powder revealed a similar final OCP as determined for massive sheet and the WA<45µm powder (Figs. 7c and 6), however with a different time dependence. No "breakdown" was observed, rather a continuous decay of the OCP level. This may be caused by the gradual dissolution of oxidized Mn- phase(s). The GA<45µm powder showed in contrast a completely different OCP-time dependence

in GST compared with the other powders and the massive sheet, Fig. 7d. The OCP started at extremely high values, between 600 and 900 mV, indicative of the presence of oxidizing surface species and/or catalysis of the cathodic reaction, as will be discussed later. In addition, "spikes" of rapidly decreasing OCP values that immediately returned to the original value were noticeable for the GA<45µm powder. These metastable breakdowns decreased in number with prolonged time after which the OCP stabilized at approximately 450 to 500 mV. A similar fluctuation in OCP has been observed for iron exposed in a 2% NaCl solution and was referred to as metastable pitting [52]. The higher stability of the Mn-phase(s), which induced a significant ennoblement in the case of the GA<45µm powder, may be related to its presence in surface oxide nanoparticles within an Fe-oxide-rich matrix, not present for the GA<4µm powder (Figs. 1-3, [39]).

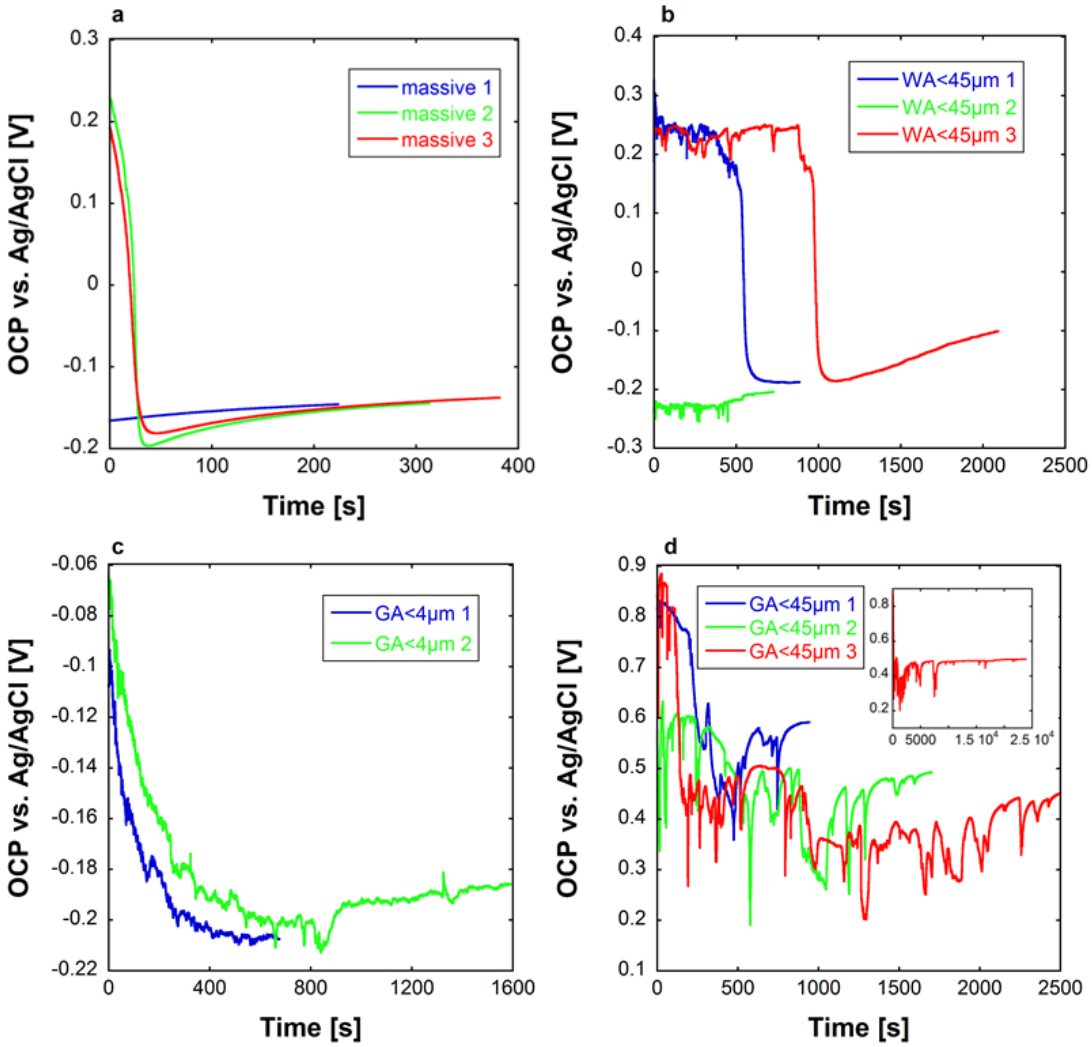

Figure 7. OCP measurements over time in gastric fluid, GST (pH 1.7): for a) massive 316L (3 replicate measurements, denoted "1", "2", and "3"), b) water atomized, WA powder particles (<45 µm, 3 replicate measurements), c) gas atomized GA powder particles (<4 µm, 2 replicate measurements), and d) GA powder particles (<45 µm, 3 replicate measurements) – inset: longer (48 h) time measurements (GA<45µm 3).

3.3. Cyclic voltammetry measurements – electrochemical surface oxide characterization

In order to obtain more detailed information on the speciation/oxidation states of metals within the surface oxide, cyclic voltammetry measurements were conducted by using CPE, Fig. 8. Detailed results have recently been reported for the GA<4μm, the GA<45μm, and the WA<45μm powders [39], but not in relation to powder particles manually generated via surface abrasion of massive sheet, used as a reference. As previously discussed [39], the first cathodic peak (C1) was assigned to adsorbed oxygen [35]. Tetravalent Mn was clearly observed in the case of the GA<4μm powder, with a peak at -0.41 $V_{Hg/HgO}$ (C3), and a corresponding anodic peak at -0.11 V (A5), as described in the literature [35, 43]. The GA<45μm powder revealed slightly shifted peaks occurring at -0.44 V and -0.01 V (C4/A6), respectively, which indicate the presence of a different Mn-containing phase more difficult to reduce. This may be due to the presence of the Mn-rich oxide nanoparticles within a protective Fe-oxide matrix, Figs. 1-3 [39]. Trivalent Fe was undoubtedly present on all powders, as judged from the cathodic peak at -1.12 V (C10), a corresponding anodic peak at about -0.9 V (A1), and possibly also the small peaks (GA<4μm powder) at -0.78 V (A2) and about -0.7 V [35, 43, 53]. The oxidation of trivalent to hexavalent Cr was most probably reflected in the strong anodic peak at 0.2 V (A7) [54], a peak observed on all powders except the WA<45μm powder. As previously discussed [39], several Mn-oxides of tri- or tetravalent oxidation states were assigned for the GA<4μm powder based on literature data [35] including β-MnO_2 with cathodic peaks at -0.54 V (C5) and -0.98 V (C8), and corresponding anodic peaks at -0.33 and -0.11 V (A4 and A5) [35]. In addition to β-MnO_2, either Mn_3O_4 (C8, A4, and A5) [35], or Mn_2O_3 (C3, C8, A4, and A5) [35], or both were present on the surface. The presence of γ-MnO_2 and MnOOH was however not possible based on literature data [35, 55]. The distinct peak C7 (-0.68 V) observed for the WA<45μm powder (not for the GA powders) was not reflected in any anodic peak. This indicates that the reduction of this phase resulted in the formation of another phase not possible to oxidize at given conditions. Considering the oxidation/reduction possibilities of the surface products at pH 13.1-13.3, only the presence of hexavalent Cr, reduced to $Cr(OH)_4^-$ (aq) remained a possible explanation. This observation and the complete absence of the peak corresponding to trivalent Cr-oxide (A7) suggested that Cr was predominantly present as hexavalent Cr in the oxide of the WA<45μm powder. Also the estimation of the transformed mass, based on the peak area and an assumed 3-electron transition (hexavalent Cr→trivalent Cr), as presented in [39], suggested in addition that hexavalent Cr in contrast to e.g. Mn or Fe remained the only possible explanation. This observation was furthermore supported by higher XPS binding energies for the Cr-peak of the WA<45μm powder compared to the GA powders lacking this CV oxidation peak. The distinct cathodic peak C6 (-0.58 V) observed for abraded "massive" particles was not reflected in any anodic peaks and is at present unknown, however, any contribution of contaminants from the diamond file cannot be excluded. When analyzing an abraded 316L massive sheet as reference, this peak was not observed, only the peaks C10, A1, and A7, corresponding to trivalent Fe and Cr, respectively.

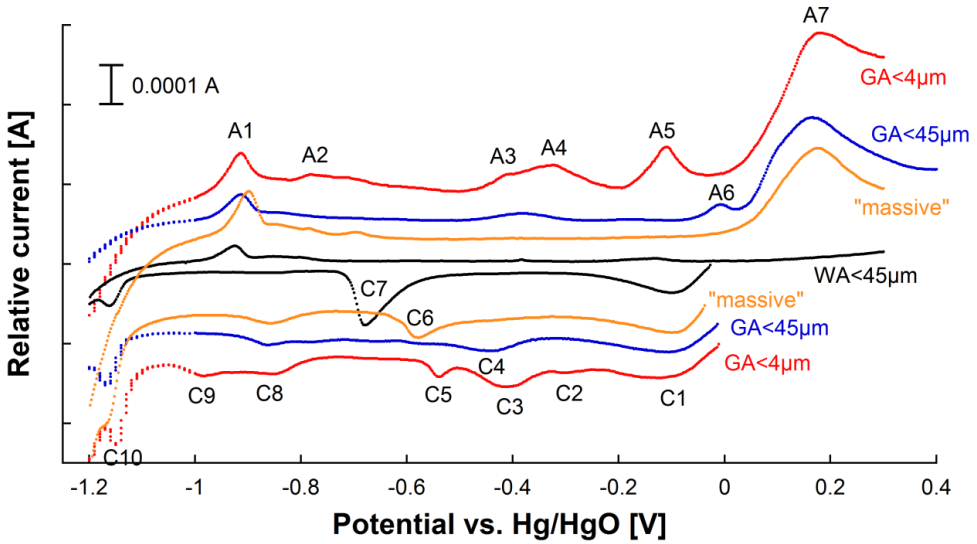

Figure 8. Gas-atomized 316L particles sized GA<4µm and GA<45µm, water-atomized 316L particles WA<45µm, and "massive" particles, measured by means of the graphite paste electrode (CPE) in 8 M NaOH. The particle concentrations in the graphite paste were 3.2 mg ("massive"), 11.6 mg (WA<45µm), 6 mg (GA<4µm), and 20 mg (GA<45µm), added to 100 mg graphite powder, respectively. The spectra are off-set for clarity.

Since the presence of MnO_2 and/or other tri-or tetravalent Mn-phases was not easily explained from a thermodynamic perspective [39], it was concluded that its formation during the atomization process must be of kinetic nature [39]. The strong increased OCP value (a significant ennoblement) could be explained by the presence of tri- and/or tetravalent Mn-species. Beside numerous reports of MnO_2-induced ennoblement of stainless steel in freshwater [47-51], MnO_2 is known to catalyze the oxygen reduction reaction and thereby increase the OCP [56-57]. This catalytic property was proposed to be caused by chemical oxidation of trivalent surface Mn-ions generated by the discharge (i.e., reduction) of MnO_2 [56].

Previous surface oxide characterization by means of confocal Raman microscopy of the GA<4µm, GA<45µm, and WA<45µm powder particles [39], suggested the following surface oxide constituents of the inert-gas-atomized powders: Cr_2O_3, α-Fe_2O_3, and possibly Fe_3O_4, Mn_3O_4, MnO_2, $MnFe_2O_4$, $MnCr_2O_4$, $FeCr_2O_4$, and δ-FeOOH. Except for possibly Fe_3O_4 or Mn_3O_4, these components were not constituents of the surface oxide of the WA<45µm powder predominantly composed of silicate-rich phases. No chromate-species were observed in any of the powders, suggesting that the hexavalent Cr-species observed in the case of the WA<45µm powder was incorporated in the silicate phase.

3.4. Implications of the surface oxide characteristics for the corrosion resistance

From the above discussed influence of trivalent and/or tetravalent Mn-oxide surface species on the OCP of the particles followed the question whether this ennoblement would influence the overall corrosion properties of the powders. Previous findings have shown that such an ennoblement may

induce pitting corrosion if the OCP exceeds a certain pitting potential [47]. However, the stainless steel grade 316L (molybdenum-containing) of this study is considered as a pitting corrosion resistant material [58].

To investigate the influence of ennoblement on corrosion, potentiodynamic anodic polarization curves were recorded for all powders immobilized on the PIGE, in different solutions. 0.03 M HCl was found sufficiently aggressive to elucidate differences in corrosion properties between the powders, Fig. 9. It should be underlined that the exact area of the powders actually in electrical contact with the PIGE is unknown. The current height should hence not be interpreted, only the curve shapes and features. The results clearly show that OCP was not directly correlated to the corrosion properties determined from the polarization curves, Fig. 9. The GA<4µm powder particles were relatively unaffected with no features corresponding to metastable pitting or stable pitting. Instead the typical oxidation peak between 1 and 1.2 V (Ag/AgCl) occurred as observed in the case of no pitting corrosion for particles [36] and assigned to the thickening of the inner trivalent Fe and Cr oxide layer [59]. The WA<45µm powder particles presented a higher pitting corrosion susceptibility, indicated by numerous metastable pitting features throughout the entire potential range (OCP - +1.2 V). The GA<45µm particles revealed furthermore strong corrosion upon initial polarization, however, with only few features at high potentials (0.9-1.2 V), indicative of the activation and dissolution of some more active particles upon polarization. Previous findings have shown a predominantly ferritic structure of the GA<4µm powder, i.e. with ferro-magnetic properties, despite its austenitic composition, whereas the GA<45µm powder could be divided into a larger non-magnetic (austenitic) and a small magnetic (ferritic) particle fraction. The average particle size of this magnetic fraction was hence smaller (approx. <10 µm) than the entire fraction of the GA<45 µm powder [14]. To investigate any influence of the structure, the magnetic and non-magnetic particle fraction of the GA<45µm powder were investigated separately to display potential differences in corrosion properties, Fig. 9. The results clearly showed that the polarization curves of the GA<45µm particles primarily were governed by the magnetic (i.e., smaller) particle fraction, whereas the non-magnetic (i.e. larger and austenitic) particle fraction revealed a significantly smoother polarization curve with a similar oxidation peak as observed for the GA<4µm powder. It has previously been suggested that this metastable ferritic structure of the undercooled GA stainless steel powder particles deteriorates its corrosion resistance [13, 41].

It should be underlined that the smaller sized (magnetic) fraction most probably revealed a higher amount of Mn in the surface oxide (not determined), but showed a lower OCP value compared with the austenitic particle fraction. This observation, in addition to the fact that the GA<4µm powder particles with the highest amounts of Mn-oxides in the surface oxide displayed a lower OCP value in most aggressive solutions, emphasizes the importance of the stability of the oxidized Mn-phase for the OCP level, rather than its relative surface quantity. Previous findings show that a MnO_2 surface coverage of only 0.1-0.2% is sufficient to increase the OCP values to similar values as a full surface coverage [48]. The presence of Mn-rich oxide nanoparticles, also enriched in S, observed for the GA<45µm particles [39] may explain their higher pitting corrosion susceptibility compared with the smaller sized ferritic GA<4µm particles without such oxide nanoparticles.

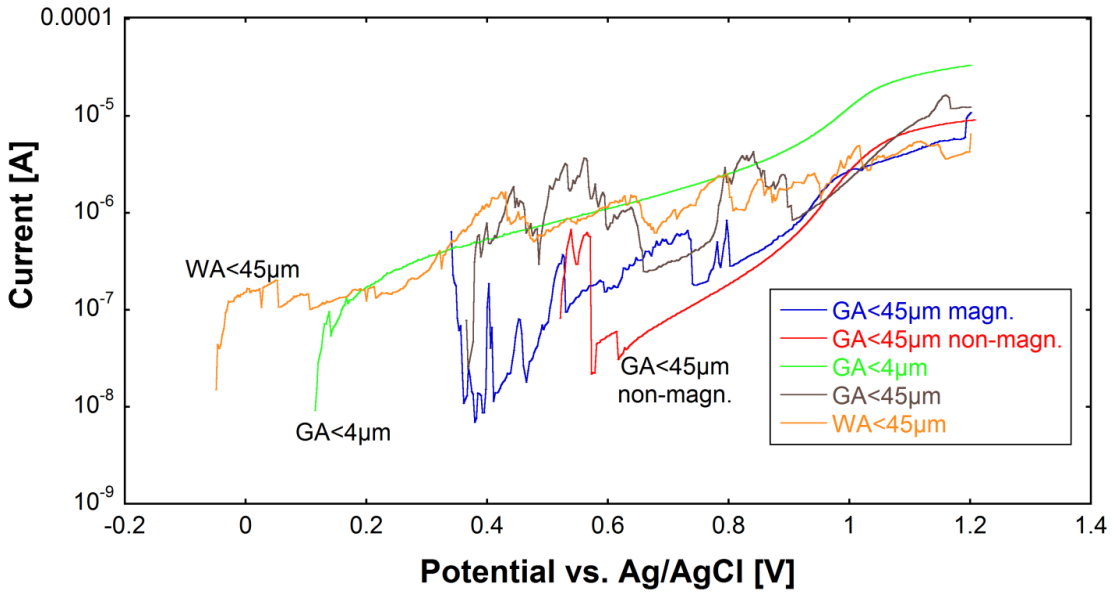

Figure 9. Anodic polarization curves in 0.03 M HCl (5 g/L 25% HCl) for gas-atomized particles (GA<4µm and GA<45µm), gas-atomized particles < 45 µm separated into non-magnetic (GA<45µm non-magn.) and magnetic particles (GA<45µm magn.), and water-atomized particles (WA<45µm). Average curves are shown for 2 replicate measurements and 4 replicate measurements (WA<45µm), in the range between the lowest OCP value among the replicate measurements and 1200 mV.

3.5. Implications of the surface oxide characteristics on the metal release process

It is difficult to predict any metal release at OCP conditions from electrochemical investigations alone, since also chemical (and/or physical) dissolution processes contribute to the metal release process [13]. The release of Fe, Cr, Ni, and Mn, has previously been investigated for all powders of this study into different synthetic body fluids and reference solutions using atomic absorption spectroscopy. Generally, all elements are increasingly released with increasing time, solution acidity and solution complexation capacity [8, 13, 60]. Also, proteins induce a significantly enhanced metal release, however, less enhanced for powders compared with massive sheet of 316L [60]. Normalized on the surface area of the particles, similar amounts of Fe, Cr, and Ni were released into PBS or PBS containing proteins (bovine serum albumin or lysozyme) [60]. This indicates that the proposed difference in oxidation state of Cr in the surface oxide of the WA<45µm particles compared with the GA particles (c.f. discussion above) was not reflected in the released amount of Cr. The presence of hexavalent chromium (not as chromate based on Raman measurements [39]) is theoretically possible within a spinel phase, as reported for the cation-doped spinel of $LiMn_2O_4$ [61]. Moreover, it has been shown that hexavalent Cr can occur in a gaseous form at high (>600°C) temperatures, but only in the presence of water vapor, not in dry gas [62]. This may explain the observed difference in chromium speciation between the gas- and water-atomized powders.

Mn was only released from the GA powders [60]. The GA powders showed in a previous study that the release of metals was strongly dependent on the solution acidity and its complexation capacity [13]. The GA<4µm powder released significantly less amounts of metals in non-aggressive (low

acidity and complexation capacity) solutions, but significantly more in aggressive solutions, compared with the GA<45μm powder [13]. The release of Fe was by far more dependent on the complexation capacity and the acidity of the solution compared with Cr and Ni, whereas the release of Mn was more dependent on the solution pH [13]. This dependence was significantly more pronounced for the GA<4μm powder, indicative of a less stable surface oxide in complexing or acidic environments. This observation is in agreement with the investigation of the effect of solution and pH on the OCP level (Figs. 5-6), findings that showed that the ennoblement induced by MnO_2 (and/or tri- or tetravalent Mn) for the GA<4μm powder only was valid in non-aggressive and neutral/alkaline solutions. On the other hand, no indication of any correlation between the pitting corrosion properties of the GA<4μm powder (Fig. 9) and the extent of metal release was evident. This indicates a partial dissolution of the surface oxide that does not result in pitting breakdown. Enhanced metal release in complexing solutions of the GA<4μm powder compared with the GA<45μm powder may be explained by the amorphous surface oxide, c.f. TEM measurements, which enables stronger complexation to ligands and detachment of complexes [63]. For both GA powders, a complete dissolution of Mn in the surface oxide was evident after immersion in highly complexing (citric acid, pH 4.5) solutions for 24 h. This was coupled with a local oxidation of the trivalent Cr-oxide to a stable (insoluble) hexavalent Cr-phase [13]. The presence of small amounts of Ni (determined by means of AES) at the utmost surface oxide (Fig. 1) may explain previously observed nickel release without strong indications of pitting corrosion (Fig. 9) [13].

4. SUMMARY

The focus of this study has been to employ a multi-analytical investigation combining bulk and surface analytical techniques with electrochemical methods to characterize the surface oxide of inert-gas- and water-atomized stainless steel AISI 316L powder and thereby enable an in-depth understanding of its importance for metal release and corrosion processes as well as on the ennoblement (positive shift in potential) induced by catalytic properties of MnO_2 and/or other tri- or tetravalent manganese oxides present in the surface oxide.

Oxidized Mn was strongly enriched in the outermost surface oxide of the inert gas-atomised (GA) powders, an effect increasing with decreasing particle size. Oxidized Si (as silicate) was strongly enriched at the surface of the water-atomised (WA) powder (<45 μm). Mn was predominantly present in its tetravalent oxidation state in the gas-atomized powders. Mn-rich oxide nanoparticles (20-100 nm) with equal amounts of Fe and small amounts of S were present at the utmost surface of the GA<45μm powder particles predominantly composed of Fe_2O_3. No oxide nanoparticles were observed at the GA<4μm particle surface, most probably as a result of rapid cooling rates during atomization.

AES depth profiles revealed in addition the enrichment of Cr in an inner layer of the oxide for both GA powders, whereas Mn and S were enriched in the Fe_2O_3-rich utmost surface oxide. AES depth profiles and TEM measurements revealed an oxide thickness of approximately 2 nm (by means of AES, slightly thicker observed by means of TEM) for both GA powders (<4 and <45 μm). The oxide was amorphous in the case of the GA<4μm powder, and partially crystalline in the case of the GA<45μm powder.

A strong ennoblement of up to 800 mV, depending on solution, was observed for the GA powder particles and was induced by the presence of tri- and/or tetravalent Mn oxide(s) due to their catalytic oxygen reduction properties. The ennoblement was not correlated to the Mn content in the surface oxide, but to its phase stability. In the case of the GA<45μm powder particles, for which Mn was enriched in oxide nanoparticles at the surface, the induced ennoblement by the Mn-oxide phase was significantly more stable over time in aggressive solutions compared with observations for the GA<4μm powder, despite the lower total Mn content in the outermost particle surface.

The total amount of Mn on the surface did not significantly influence the pitting corrosion behavior in contrast to the bulk structure (austenite or ferrite). However, it is proposed that the Mn-rich oxide nanoparticles in the case of the GA<45μm powder resulted in higher pitting corrosion. The metal release at OCP conditions in different solutions was strongly dependent on the oxide properties, and coupled to the oxidation of Cr induced by tri- or tetravalent Mn in complexing media in the case of the GA powders.

The WA<45μm powder differed in many aspects from the GA powders. In contrast to only trivalent Cr-oxide in the surface oxide of the GA powders (confirmed by several techniques), the WA powder revealed oxidized Cr to be in the hexavalent state (confirmed not as chromate), most probably within a silicate-rich surface oxide. The WA<45μm powder revealed a higher corrosion susceptibility, no OCP ennoblement (due to the absence of tri- and/or tetravalent Mn-species in the surface oxide), and similar amounts of released Fe , Cr and Ni at OCP conditions as observed for the GA powders at given conditions.

It was clearly shown that the surface oxide composition and speciation of differently sized inert-gas-atomized and water-atomized 316L powder particles are unique and strongly connected to the atomization process. The bulk composition alone is hence a too rough estimation of metal release and/or corrosion properties of stainless steel powders.

ACKNOWLEDGEMENTS

Experimental help from Maria-Elisa Karlsson, Dagny Ullmann, Claudio Baldizzone, Dr. Wubashet Sahle (Functional Materials Division, KTH), and Oskar Karlsson (Swerea KIMAB, Sweden), travel grants from Jernkontoret, Sweden, and Björn foundation, Sweden, and financial help by Cusanuswerk, Germany (for Yolanda Hedberg), are highly acknowledged. Yolanda Hedberg and Inger Odnevall Wallinder are members of the Stockholm Particle Group, an operative network between three universities in Stockholm: Karolinska Institutet, Royal Institute of Technology and Stockholm University, supported by the Swedish Research Councils VR and Formas.

References

1. EU, *REACH in brief*. 2007, European Commission Environment Directorate General: ec.europa.eu/environment/chemicals/reach/pdf/2007_02_reach_in_brief.pdf.
2. EC, *Regulation (EC) No 1907/2006 of the European Parliament and of the Council of 18 December 2006 concerning the Registration, Evaluation, Authorisation and Restriction of Chemicals (REACH), establishing a European Chemicals Agency, amending Directive 1999/45/EC and repealing Council Regulation (EEC) No 793/93 and Commission Regulation (EC) No 1488/94 as well as Council Directive 76/769/EEC and Commission Directives 91/155/EEC, 93/67/EEC,*

93/105/EC and 2000/21/EC, E. Council, Editor. 2006: Official Journal of the European Union. p. L396:L136/133.
3. Y. Hedberg: *Environmental and health aspects of corrosion–importance of chemical speciation*, PhD thesis, Royal Institute of Technology (KTH), Stockholm, Sweden, 2010.
4. Y. Hedberg, J. Gustafsson, H. L. Karlsson, L. Möller, and I. Odnevall Wallinder, *Part. Fibre Toxicol.*, 7:23 (2010).
5. Y. Hedberg, K. Midander, and I. Odnevall Wallinder, *Integrat. Environ. Assess. Manag.*, 6(3) (2010) 456.
6. Y. Hedberg and I. Odnevall Wallinder, *Mater. Corros.*, 63(6) (2012) 481.
7. K. Midander: *Metal Particles-Hazard Or Risk?: Elaboration and Implementation of a Research Strategy from a Surface and Corrosion Perspective*, PhD thesis, Royal Institute of Technology (KTH), Stockholm, Sweden, 2009.
8. K. Midander, A. de Frutos, Y. Hedberg, G. Darrie, and I. Odnevall Wallinder, *Integrat. Environ. Assess. Manag.*, 6(3) (2010) 441.
9. K. Midander, J. Pan, I. Odnevall Wallinder, and C. Leygraf, *J. Environ. Monitor.*, 9 (2007) 74.
10. T. Santonen, H. Stockmann-Juvala, I. Odnevall Wallinder, G. Darrie, and A. Zitting: *Use of read-across in the health risk assessment of ferro-chromium alloys under REACH*, The Twelth International Ferro Alloy Congress (INFACON XII), Helsinki (FI), 6-9 June 2010, 2010.
11. T. Santonen, H. Stockmann-Juvala, and A. Zitting: *REVIEW ON TOXICITY OF STAINLESS STEEL*, Finnish Institute of Occupational Health, Helsinki, Finland (2010), http://www.ttl.fi/en/publications/Electronic_publications/Documents/Stainless_steel.pdf.
12. UN, *The Globally Harmonized System of Classification and Labelling of Chemicals, Annex 10, Guidance on transformation/dissolution of metals and metal compounds in aqueous media*. 2009.
13. Y. Hedberg, J. Hedberg, Y. Liu, and I. Odnevall Wallinder, *BioMetals*, 24(6) (2011) 1099.
14. Y. Hedberg, O. Karlsson, P. Szakalos, and I. Odnevall Wallinder, *Mater. Lett.*, 65(14) (2011) 2089.
15. H. Stockmann-Juvala, Y. Hedberg, N. K. Dhinsa, D. R. Griffiths, P. N. Brooks, A. Zitting, I. Odnevall Wallinder, and T. Santonen, (submitted manuscript).
16. T. Tunberg and L. Nyborg, *Powder Metall.*, 38(2) (1995) 120.
17. L. Nyborg, T. Tunberg, and P. X. Wang, *Metal Powder Report*, 45(11) (1990) 750.
18. M. Norell, L. Nyborg, and I. Olefjord: 'Reactions during atomization of martensitic stainless steel', San Francisco, CA, USA, 1992, Publ by Metal Powder Industries Federation, 41.
19. L. Nyborg and I. Olefjord, *Key Eng. Mat.*, 29-31 (1989) 9.
20. E. Hryha, C. Gierl, L. Nyborg, H. Danninger, and E. Dudrova, *Appl. Surf. Sci.*, 256(12) (2010) 3946.
21. P. Bracconi and G. Gasc, *Metall. Mater. Trans. A*, 25(3) (1994) 509.
22. P. Bracconi and L. Nyborg, *Appl. Surf. Sci.*, 133(1–2) (1998) 129.
23. T. Kelly, M. Cohen, and J. van der Sande, *Metall. Mater. Trans. A*, 15(5) (1984) 819.
24. T. Volkmann, D. Herlach, and W. Löser, *Metall. Mater. Trans. A*, 28(2) (1997) 461.
25. W. Löser, T. Volkmann, and D. M. Herlach, *Mat. Sci. Eng. A*, 178(1-2) (1994) 163.
26. W. Löser and D. Herlach, *Metall. Mater. Trans. A*, 23(5) (1992) 1585.
27. A. Doménech, M. T. Doménech-Carbó, T. Pasies, and M. C. Bouzas, *Electroanal.*, 23(12) (2011) 2803.
28. F. Scholz, U. Schröder, and R. Gulaboski: *Electrochemistry of immobilized particles and droplets*, Springer Verlag, (2005).
29. T. Grygar, P. Bezdicka, D. Hradil, A. Domenech-Carbo, F. Marken, L. Pikna, and G. Cepria, *Analyst*, 127(8) (2002) 1100.
30. M. Mouhandess, F. Chassagneux, B. Durand, Z. Sharara, and O. Vittori, *J. Mater. Sci.*, 20(9) (1985) 3289.
31. M. T. Mouhandess, F. Chassagneux, and O. Vittori, *J. Electroanal. Chem.*, 131(0) (1982) 367.

32. M. T. Mouhandess, F. Chassagneux, O. Vittori, A. Accary, and R. M. Reeves, *J. Electroanal. Chem.*, 181(1–2) (1984) 93.
33. P. Encinas, L. Lorenzo, M. L. Tascón, M. D. Vázquez, and P. Sánchez-Batanero, *J. Electroanal. Chem.*, 371(1–2) (1994) 161.
34. P. Encinas Bachiller, M. L. Tascon Garcia, M. D. Vazquez Barbado, and P. Sanchez-Batanero, *J. Electroanal. Chem.*, 367(1–2) (1994) 99.
35. F. Chouaib, O. Cauquil, and M. Lamache, *Electrochim. Acta*, 26(3) (1981) 325.
36. Y. Hedberg, S. Virtanen, and I. Odnevall Wallinder, *Int. J. Electrochem. Sci.*, in press (this issue, following article).
37. K. Midander, J. Pan, and C. Leygraf, *Corros. Sci.*, 48(9) (2006) 2855.
38. P. Anderson and W. Swartz Jr, *Inorg. Chem.*, 13(9) (1974) 2293.
39. Y. Hedberg, P. Linhardt, M. Norell, J. Hedberg, P. Szakálos, and I. Odnevall Wallinder, *Powder Metall.*, in press.
40. M. Norell, L. Nyborg, T. Tunberg, and I. Olefjord, *Surf. Interf. Anal.*, 19(1-12) (1992) 71.
41. C. Baldizzone: 'Investigations of passivity and reactivity of alloy particles, effects of sonication and particle size', PhD thesis, Royal Institute of Technology (KTH), Stockholm, 2010.
42. D. R. Lide, ed. *CRC handbook of chemistry and physics*, 1973, Boca Raton, USA, CRC Press Inc.
43. P. Linhardt, *Mater. Sci. For.*, 289 (1998) 1267.
44. H. Nesbitt and D. Banerjee, *Am. Mineral.*, 83(3-4) (1998) 305.
45. L. Nyborg and I. Olefjord, *Powder Metall. Int.*, 20(2) (1988) 11.
46. J. J. Dunkley: *Progress in Powder Metallurgy*, 39, Metal Powders Industries Federation, Princeton, NJ (1982).
47. W. H. Dickinson, F. Caccavo Jr, and Z. Lewandowski, *Corros. Sci.*, 38(8) (1996) 1407.
48. P. Linhardt, *Biodegradation*, 8(3) (1997) 201.
49. P. Linhardt, *Mater. Corros.*, 55(3) (2004) 158.
50. P. Linhardt, *Mater. Corros.*, 61 (2010) 1034.
51. C. Marconnet, C. Dagbert, M. Roy, and D. Féron, *Corros. Sci.*, 50(8) (2008) 2342.
52. M. Hashimoto, S. Miyajima, and T. Murata, *Corros. Sci.*, 33(6) (1992) 885.
53. H. Neugebauer, G. Nauer, N. Brinda-Konopik, and G. Gidaly, *J. Electroanal. Chem.*, 122(0) (1981) 381.
54. T. Grygar and P. Bezdička, *J. Solid State Chem.*, 3(1) (1998) 31.
55. J. McBreen, *Electrochim. Acta*, 20(3) (1975) 221.
56. Y. Cao, H. Yang, X. Ai, and L. Xiao, *J. Electroanal. Chem.*, 557 (2003) 127.
57. F. H. B. Lima, M. L. Calegaro, and E. A. Ticianelli, *J. Electroanal. Chem.*, 590(2) (2006) 152.
58. A. J. Sedriks: *Corrosion of Stainless Steels*, John Wiley & Sons, Inc., New York (1996).
59. V. Maurice, W. P. Yang, and P. Marcus, *J. Electrochem. Soc.*, 145(3) (1998) 909.
60. N. Mazinanian: 'Influence of microstructure and proteins on the metal release of micron-sized stainless steel particles', PhD thesis, Royal Institute of Technology, Stockholm, 2012.
61. C. Wu, Z. Wang, F. Wu, L. Chen, and X. Huang, *Solid State Ionics*, 144(3) (2001) 277.
62. H. Asteman, K. Segerdahl, J. E. Svensson, and L. G. Johansson, *Mater. Sci. For.*, 369-372 (2001) 277.
63. R. F. Carbonaro, B. N. Gray, C. F. Whitehead, and A. T. Stone, *Geochim. Cosmochim. Acta*, 72(13) (2008) 3241.